

## Full length article

Coupled diffusion-deformation multiphase field model for elastoplastic materials applied to the growth of  $\text{Cu}_6\text{Sn}_5$ Johan Hektor<sup>a,\*</sup>, Matti Ristinmaa<sup>a</sup>, Håkan Hallberg<sup>a</sup>, Stephen A. Hall<sup>a,c</sup>, Srinivasan Iyengar<sup>b</sup><sup>a</sup> Division of Solid Mechanics, Lund University, Box 118, 221 00 Lund, Sweden<sup>b</sup> Division of Materials Engineering, Lund University, Box 118, 221 00 Lund, Sweden<sup>c</sup> European Spallation Source, Box 176, 221 00 Lund, Sweden

## ARTICLE INFO

## Article history:

Received 17 December 2015

Received in revised form

27 January 2016

Accepted 7 February 2016

Available online xxx

## Keywords:

Intermetallic compounds

 $\text{Cu}_6\text{Sn}_5$ 

Phase field model

Finite element method

## ABSTRACT

A coupled diffusion-deformation, multiphase field model for elastoplastic materials is presented. The equations governing the evolution of the phase fields and the molar concentration field are derived in a thermodynamically consistent way using microforce balance laws. As an example of its capabilities, the model is used to study the growth of the intermetallic compound (IMC)  $\text{Cu}_6\text{Sn}_5$  during room-temperature aging. This IMC is of great importance in, e.g., soldering of electronic components. The model accounts for grain boundary diffusion between IMC grains and plastic deformation of the microstructure. A plasticity model with hardening, based on an evolving dislocation density, is used for the Cu and Sn phases. Results from the numerical simulations suggest that the thickness of the IMC layer increases linearly with time and that the morphology of the IMC gradually changes from scallop-like to planar, consistent with previous experimental findings. The model predicts that plastic deformation occurs in both the Cu and the Sn layers. Furthermore, the mean value of the biaxial stress in the Sn layer is found to saturate at a level of  $-8$  MPa to  $-10$  MPa during aging. This is in good agreement with experimental data.

© 2016 Acta Materialia Inc. Published by Elsevier Ltd. All rights reserved.

## 1. Introduction

Over the past years phase field modeling has evolved into a powerful tool for computational materials science. One advantage of phase field models is that there is no need to explicitly track the position of interfaces during microstructural evolution. Instead, the position of the interfaces is implicitly given by the evolution of the phase field variables used to describe the microstructure. This makes it possible to simulate complex polycrystalline microstructures without making assumptions on, e.g., the shape of the grains [1]. Phase field models have been used to study, for example, solidification processes and dendritic growth [2,3], recrystallization [4], and martensitic phase-transformation [5]. Another phenomena to which phase field modeling is well adapted is growth of intermetallic compounds (IMC). The focus of the present work is the IMC in the Cu–Sn system. These IMC are of great importance due to

their role in soldering of electronic components. The recent transition to lead-free solders, driven by environmental concerns and legislation, have further increased the interest for the Cu–Sn system, both from experimental [6–13] and modeling [14–18] perspectives.

During a soldering process, a layer of the intermetallic compound  $\text{Cu}_6\text{Sn}_5$  ( $\eta$ -phase) will form at the interface between the Cu substrate and the liquid solder [9]. A small amount of IMC is necessary to achieve sufficient bonding between the substrate and the solder. However, in the presence of too much IMC, the mechanical properties of the solder joint will degrade due to the brittleness of the intermetallic phase [19]. The thickness of the IMC will increase during aging and the growth of the  $\text{Cu}_6\text{Sn}_5$  phase will introduce stresses in the surrounding microstructure [8]. These stresses are believed to be responsible for another reliability concern in the electronics industry, namely the growth of tin whiskers [20].

The formation and growth of intermetallic compounds in the Cu–Sn system has been previously studied using the phase field method. A one-dimensional model of the growth of  $\text{Cu}_6\text{Sn}_5$  was

\* Corresponding author.

E-mail address: [johan.hektor@solid.lth.se](mailto:johan.hektor@solid.lth.se) (J. Hektor).

developed by Umantsev in Ref. [17]. In this model the phase fields represent ordering and crystallization rather than individual grains. Huh et al. [14] developed a model for simulating growth of  $\text{Cu}_6\text{Sn}_5$  between a Cu substrate and molten solder. Based on the model by Huh and coworkers, several additional studies have been presented, e.g. Refs. [15,16]. None of these models, however, take the mechanical behavior of the material into account. In Ref. [18], the stress build-up caused by the growth of IMC is simulated using the finite element method. The model in Ref. [18] is uncoupled and only deformation is taken into account while the growth of IMC is added based on curve fitting of experimental data.

In this paper, we present a coupled diffusion-deformation, multiphase field model capable of simulating both the growth of the  $\text{Cu}_6\text{Sn}_5$  phase and the associated build-up of stresses. The equations governing the evolution of the simulated microstructure are derived in a thermodynamically consistent way using the concept of microforces [21,22] and the constitutive framework developed by Ammar et al. [23]. The model is used to study the growth behavior of  $\text{Cu}_6\text{Sn}_5$  during isothermal aging at room temperature.

The paper is structured in the following way: In Section 2 the multiphase field model is derived, starting from a dissipation inequality and a postulated free energy. In Section 3 and Section 4 numerical aspects of the model and the choice of model parameters are discussed. Results from the simulations are presented in Section 5. The paper is closed with some concluding remarks in Section 6.

## 2. Multiphase field model

In multiphase field models a polycrystal microstructure is represented by a set of non-conserved phase fields  $\phi = (\phi_a(t, \mathbf{X}), \phi_b(t, \mathbf{X}), \dots, \phi_n(t, \mathbf{X}))$ , where each phase field represents one grain in the microstructure. The phase fields are functions of time,  $t$ , and spatial coordinates,  $\mathbf{X}$ . Grain boundaries are taken as the regions where two or more phase field variables vary smoothly between 0 and 1. The smooth variation occurs over some distance, creating a diffuse interface region. Based on the properties of each phase present at the interface, the material properties of the interface region can be estimated using the interpolation function introduced in Ref. [15]:

$$h_i(\phi) = \frac{\phi_i^2}{\sum_j \phi_j^2}, \quad (1)$$

where the sum in the denominator is taken over all phase fields, i.e.  $j = 1 \dots n$ .

To simulate diffusion, conserved field variables  $\mathbf{x} = (x_a(t, \mathbf{X}), x_b(t, \mathbf{X}), \dots, x_n(t, \mathbf{X}))$ , representing the molar fraction in each grain is used. The molar fraction fields are related to the global molar concentration field  $c$  through

$$c = \sum_n h_n \frac{x_n}{V_m}, \quad (2)$$

where the interpolation function  $h_i$  in (1) is used to interpolate between the molar fraction field corresponding to each phase field and where  $V_m$  is a constant molar volume.

The derivation of the equations governing the evolution of the phase fields and the concentration field is presented below. The derivation is based on the framework developed by Ammar et al. [23]. In the present work, this framework is extended to a multiphase setting by making use of the interpolation function (1) and by formulating the free energy and other quantities as summations over all phase fields. Following [21] and [22], a system of

microforces is associated with each phase field. These forces represent configurational forces acting on the crystal lattice. The microforce system belonging to phase field  $a$  comprises an internal microstress vector  $\xi_a$  and a scalar microforce  $\pi_a$ , as well as an external microforce  $\gamma_a$ . The microforces in the other phases are defined analogously. In the same way as the Cauchy stress  $\sigma$  is energy-conjugated with the gradient of the displacement  $\nabla \mathbf{u}$ ,  $\pi_a$  and  $\xi_a$  are energy-conjugated with  $\phi_a$  and  $\nabla \phi_a$ , respectively. Each microforce system is presumed to follow a balance law, cf. [21], of the form

$$\nabla \cdot \xi_i + \pi_i + \gamma_i = 0. \quad (3)$$

The term microforce system is motivated by (3) having the same form as the equilibrium equation for the Cauchy stress,

$$\nabla \cdot \sigma + \mathbf{b} = 0, \quad (4)$$

where  $\mathbf{b}$  denotes the body force vector.

### 2.1. Dissipation inequality

Following the procedure in Ref. [23], with the enhancement that the power densities are formulated as sums over all phase fields, the first and second laws of thermodynamics result in a Clausius-Duhem inequality,

$$-\sum_i \pi_i \dot{\phi}_i + \sum_i \xi_i^T \nabla \dot{\phi}_i + \sigma : \dot{\epsilon} - \dot{f} + \mu \dot{c} - \mathbf{J}^T \nabla \mu \geq 0, \quad (5)$$

where  $\epsilon = \epsilon^e + \epsilon^* + \epsilon^p$  is the total strain, consisting of elastic strains  $\epsilon^e$ , transformation strains  $\epsilon^*$ , and plastic strains  $\epsilon^p$ . In (5), a tensorial contraction over two indices is denoted by  $(\cdot):(\cdot)$ . The chemical potential and the diffusion flux are denoted  $\mu$  and  $\mathbf{J}$  respectively and a superposed dot denotes differentiation with respect to time. The free energy density  $f = f(\phi, \nabla \phi, c, \epsilon^e, \kappa)$  is taken as a function of the set of phase fields  $\phi$ , their gradients  $\nabla \phi$ , the global concentration field  $c$ , the elastic strain  $\epsilon^e$  and a set of internal variables  $\kappa$  related to plasticity in terms of the evolving dislocation density, to be specified later on. Using the chain rule to calculate the time derivative of  $f$  and inserting it into (5) gives

$$-\sum_i \left( \pi_i + \frac{\partial f}{\partial \phi_i} \right) \dot{\phi}_i + \sum_i \left( \xi_i - \frac{\partial f}{\partial \nabla \phi_i} \right)^T \nabla \dot{\phi}_i + \left( \mu - \frac{\partial f}{\partial c} \right) \dot{c} + \left( \sigma - \frac{\partial f}{\partial \epsilon^e} \right) : \dot{\epsilon}^e + \sigma : \dot{\epsilon}^p - \mathbf{J}^T \nabla \mu - \sum_i \frac{\partial f}{\partial \kappa_i} \dot{\kappa}_i \geq 0. \quad (6)$$

To ensure that the second law of thermodynamics is fulfilled, (6) should hold for any combination of  $\phi, \nabla \phi, c, \epsilon^e$ , and  $\kappa$ . We can therefore extract state laws for the internal microstress, the chemical potential and the Cauchy stress:

$$\xi_i = \frac{\partial f}{\partial \nabla \phi_i}, \quad \mu = \frac{\partial f}{\partial c}, \quad \sigma = \frac{\partial f}{\partial \epsilon^e}. \quad (7)$$

Inserting the state laws into (6), results in the dissipation inequality

$$D = -\sum_i \pi_i^{\text{dis}} \dot{\phi}_i - \mathbf{J}^T \nabla \mu + \sigma : \dot{\epsilon}^p - \sum_i K_i \dot{\kappa}_i \geq 0, \quad (8)$$

where  $\pi_i^{\text{dis}} = \pi_i + \frac{\partial f}{\partial \phi_i}$  and  $K_i = \partial f / \partial \kappa_i$ . From the dissipation inequality it is possible to identify three dissipative processes. The first term represents the phase field dissipation, which is related to the rearrangement of atoms during the evolution of the phase fields [23]. The second term is the mass transport caused by diffusion and

the third and fourth terms represent the dissipation caused by plastic deformation. The dissipative processes are assumed to be governed by a convex dissipation potential  $\Omega = \Omega(\boldsymbol{\pi}^{dis}, \boldsymbol{\phi}, c, \boldsymbol{\nabla}\boldsymbol{\mu}, \boldsymbol{\sigma}, \boldsymbol{K})$  such that

$$\dot{\phi}_i = -\frac{\partial\Omega}{\partial\pi_i^{dis}}, \quad (9)$$

$$\boldsymbol{J} = -\frac{\partial\Omega}{\partial\boldsymbol{\nabla}\boldsymbol{\mu}}, \quad (10)$$

$$\dot{\kappa}_i = -\dot{\lambda}_i \frac{\partial\Omega}{\partial\boldsymbol{K}_i}, \quad (11)$$

$$\dot{\boldsymbol{\epsilon}}_i^p = \dot{\lambda}_i \frac{\partial\Omega}{\partial\boldsymbol{\sigma}_i}, \quad (12)$$

where  $\dot{\lambda}_i \geq 0$  is a Lagrange multiplier associated with plastic deformation. Equation (9) is the evolution equation for phase field  $i$ , the other phase fields are treated in the same way. Equation (10) represents the diffusion flux. Equations (11) and (12) describe the evolution of the internal variables in the plasticity model associated with phase field  $i$  and the evolution of the plastic strains in grain  $i$ , respectively. The free energy density  $f$  and the dissipation potential  $\Omega$  will be defined in the following sections.

## 2.2. Free energy functional

The free energy of the system is taken as the volume integral of the free energy density,

$$F = \int_V f(\boldsymbol{\phi}, \boldsymbol{\nabla}\boldsymbol{\phi}, c, \boldsymbol{\epsilon}^e, \boldsymbol{\kappa}) dV, \quad (13)$$

consisting of three separate contributions,

$$f(\boldsymbol{\phi}, \boldsymbol{\nabla}\boldsymbol{\phi}, c, \boldsymbol{\epsilon}^e, \boldsymbol{\kappa}) = f_{ch}(\boldsymbol{\phi}, c) + f_{int}(\boldsymbol{\phi}, \boldsymbol{\nabla}\boldsymbol{\phi}) + f_u(\boldsymbol{\phi}, c, \boldsymbol{\epsilon}^e, \boldsymbol{\kappa}), \quad (14)$$

where  $f_{ch}$ ,  $f_{int}$  and  $f_u$  are the chemical, interfacial, and mechanical free energy densities, respectively. The three components are detailed individually below.

### 2.2.1. Interface free energy density

Following [15], the interfacial free energy density is taken as

$$f_{int} = m f_0(\boldsymbol{\phi}) + \frac{\alpha}{2} \sum_i (\boldsymbol{\nabla}\phi_i)^2, \quad (15)$$

with  $f_0$  being a fourth order Landau polynomial of the phase fields,

$$f_0(\boldsymbol{\phi}) = \sum_i \left( \frac{\phi_i^4}{4} - \frac{\phi_i^2}{2} \right) + \sum_i \sum_{j \neq i} \frac{\beta}{2} \phi_i^2 \phi_j^2 + \frac{1}{4}. \quad (16)$$

The model parameters  $m$ ,  $\alpha$  and  $\beta$  are related to the surface energy  $\sigma_{int}$  and the width of the diffuse interface region  $\delta$  through the expressions

$$m = \frac{6\sigma_{int}}{\delta}, \quad \alpha = \frac{3\delta\sigma_{int}}{4}, \quad \beta = \frac{3}{2}. \quad (17)$$

The minima of the Landau polynomial are located in the interior of each phase field domain, i.e. where  $(\phi_a, \phi_b, \dots, \phi_n) = (1, 0, \dots, 0), (0, 1, 0, \dots, 0), \dots, (0, \dots, 0, 1)$ . In such points it holds that  $f_0 = 0$ , which means that the bulk materials do not contribute to the interface energy. Furthermore, since  $\alpha$  is a strictly

positive parameter, interfaces will always be energetically unfavorable.

### 2.2.2. Mechanical free energy

The mechanical free energy density is split into an elastic and a plastic part,

$$f_u(\boldsymbol{\phi}, c, \boldsymbol{\epsilon}^e, \boldsymbol{\kappa}) = f^e(\boldsymbol{\phi}, c, \boldsymbol{\epsilon}^e) + f^p(\boldsymbol{\phi}, c, \boldsymbol{\kappa}), \quad (18)$$

denoted by superscripts  $e$  and  $p$ , respectively. The elastic energy density is interpolated from the strain energies of all coexisting phases using the interpolation function (1),

$$f^e = \sum_i h_i f_i^e, \quad (19)$$

where  $f_i^e = \frac{1}{2}(\boldsymbol{\epsilon} - \boldsymbol{\epsilon}_i^* - \boldsymbol{\epsilon}_i^p) : \boldsymbol{D}_i : (\boldsymbol{\epsilon} - \boldsymbol{\epsilon}_i^* - \boldsymbol{\epsilon}_i^p)$  is the elastic energy of phase  $i$ . It is assumed that the total strain,  $\boldsymbol{\epsilon}$ , is the same in all coexisting phases, but each phase can have different transformation strains and plastic strains. This corresponds to the, so called, Voigt-Taylor assumption [24]. Other ways of calculating the elastic energy includes the Reuss-Sachs model, where it is assumed that the stresses in all coexisting phases are the same, i.e.  $\boldsymbol{\sigma}_i = \boldsymbol{\sigma}_j = \boldsymbol{\sigma}$ , and the Khachaturyan scheme [25], which is essentially a combination of the Reuss-Sachs and Voigt-Taylor models.

The plastic free energy is taken as

$$f^p = \sum_i h_i f_i^p = \sum_i h_i \frac{1}{2} H_i \kappa_i^2, \quad (20)$$

where  $H_i$  is the plastic hardening modulus and  $\kappa_i = \kappa_i(\bar{\rho}_i)$  is an internal hardening variable, which is a function of the normalized dislocation density  $\bar{\rho}_i$ , as will be specified later on.

A consequence of the interpolation of the mechanical free energy is that no plastic deformation is inherited from the parent phase to the newly formed phase during the phase transformation. It is also possible to formulate phase field models where the plastic deformation is inherited to the new phase. The behavior of real materials probably lies in between full inheritance of plastic deformation and no inheritance at all [26]. This intermediate behavior necessitates the development of models allowing for partial inheritance of plastic deformation, which however is beyond the scope of the present work.

### 2.2.3. Chemical free energy

Again following [15], the chemical free energy is taken as

$$f_{ch} = \sum_i h_i \frac{G_i(x_i)}{V_m}, \quad (21)$$

where  $V_m$  is the molar volume and  $G_i$  is the molar Gibbs energy of phase  $i$ , which is a function of the molar fraction  $x_i$ . In phase field modeling, the Gibbs energy of each phase is commonly approximated as a parabolic function of the molar fraction [15,23,27]. Here, a parabola of the form

$$G_i = \frac{A_i}{2}(x_i - \hat{x}_i)^2 + B_i(x_i - \hat{x}_i) + C_i \quad (22)$$

is used to approximate the Gibbs energy. Following [27], the parameters  $A_i$ ,  $B_i$  and  $C_i$  are taken as

$$A_i = \frac{d^2 \widehat{G}_i}{dx_i^2} \Big|_{x_i = \widehat{x}_i}, \quad B_i = \frac{d \widehat{G}_i}{dx_i} \Big|_{x_i = \widehat{x}_i}, \quad C_i = \widehat{G}_i \Big|_{x_i = \widehat{x}_i}, \quad (23)$$

where  $\widehat{x}_i$  is the equilibrium molar fraction of phase  $i$  and where  $\widehat{G}_i$  is the composition-dependent Gibbs energy as obtained from, e.g., thermodynamic databases. **The reason for not using  $\widehat{G}_i$  directly in the phase field model is that these functions usually involve rather complicated logarithmic terms, which may cause numerical difficulties. It will also later turn out to be convenient to take advantage of the second derivative of  $G_i$  being constant.**

### 2.3. Dissipation potential

The dissipation potential  $\Omega$  governing the dissipative processes is divided into three parts, one part for each of the dissipative processes,  $\Omega(\pi^{dis}, \phi, c, \nabla \mu, \sigma, \mathbf{K}) = \Omega_c(\nabla \mu) + \Omega_\phi(\pi^{dis}) + \Omega_u(\phi, c, \sigma, \mathbf{K})$ . The first term,  $\Omega_c$ , is the dissipation potential related to diffusion, while  $\Omega_\phi$  and  $\Omega_u$  are the potentials for the phase field and the mechanical dissipation, respectively. To ensure that the dissipation inequality (8) is fulfilled,  $\Omega_c$ ,  $\Omega_\phi$ , and  $\Omega_u$  are taken as convex functions of their arguments.

Following [23], the chemical dissipation is taken as

$$\Omega_c(\nabla \mu) = \frac{1}{2} M(\phi) (\nabla \mu)^2, \quad (24)$$

where

$$M(\phi) = \sum_i \frac{h_i}{V_m} \left( \frac{D_i}{\frac{d^2 \widehat{G}_i}{dx_i^2}} + \sum_{j \neq i} h_j M_{gb} \right) \quad (25)$$

is the mobility. In (25),  $D_i$  denotes the diffusion coefficient of grain  $i$ . Using the parabolic approximations of the Gibbs energy it is seen that  $\frac{d^2 \widehat{G}_i}{dx_i^2} = A_i$  is a constant, which makes the mobility independent of composition. The second term in (25) is included to take into account the higher diffusion rate in grain boundaries, compared to in the bulk material. The additional contribution to the mobility of a grain boundary between grains  $i$  and  $j$  is taken as

$$M_{gb} = 3 \frac{D_{gb}}{h_i A_i + h_j A_j} \frac{\delta_{gb}}{\delta}. \quad (26)$$

It is assumed that all grain boundaries have the same diffusion coefficient,  $D_{gb}$ , and width,  $\delta_{gb}$ .

The phase field dissipation is taken as

$$\Omega_\phi(\pi^{dis}) = \frac{1}{2} L(\phi) \sum_i (\pi_i^{dis})^2 = \frac{1}{2} L(\phi) \sum_i \left( \pi_i + \frac{\partial f}{\partial \phi_i} \right)^2, \quad (27)$$

where, following [15], the kinetic coefficient  $L(\phi)$  is

$$L(\phi) = \frac{\sum_i \sum_{j \neq i} L_{ij} \phi_i^2 \phi_j^2}{\sum_i \sum_{j \neq i} \phi_i^2 \phi_j^2}. \quad (28)$$

For diffusion controlled grain boundary migration,  $L_{ij}$  is taken as

$$L_{ij} = \frac{2mV_m}{3\alpha(x_i^{eq} - x_j^{eq})^2} \frac{M_i + M_j}{2}, \quad (29)$$

where  $M_i = D_i/A_i$  and  $M_j = D_j/A_j$  are the mobilities and  $x_i^{eq}$  and  $x_j^{eq}$  are the equilibrium molar fractions of phases  $i$  and  $j$  respectively.

The mechanical contribution to dissipation is due to the plastic

strains. A local plastic dissipation potential  $\Omega_{u,i}(c, \sigma_i, K_i)$  is associated with each phase field. The total plastic dissipation is then obtained, using the interpolation function, as

$$\Omega_u(\phi, c, \sigma, \mathbf{K}) = \sum_i h_i \Omega_{u,i}(c, \sigma_i, K_i). \quad (30)$$

This treatment of the plastic dissipation allows for different phases to follow different constitutive laws. In this work it is assumed that the IMC is purely elastic, i.e.  $\Omega_{u,IMC} = 0$ , and that the plastic behavior of the Cu and Sn phases is described by an isotropic hardening von Mises model. Taking the derivatives of  $\Omega_{u,i}$  with respect to  $K_i$  and  $\sigma_i$  should, according to Equations (11) and (12), result in  $\dot{\kappa}_i$  and  $\dot{\epsilon}_i^p$ . For isotropic von Mises plasticity,  $\Omega_{u,i}$  is taken as the yield function  $g_i$ , i.e.

$$\Omega_{u,i} = g_i = \sigma_i^{eff} - \sigma_i^y(\kappa_i), \quad (31)$$

with the additional Karush-Kuhn-Tucker relations  $g_i \leq 0$ ,  $\dot{\lambda}_i \geq 0$  and  $g_i \dot{\lambda}_i = 0$ . The effective stress and the initial yield stress are denoted  $\sigma_i^{eff}$  and  $\sigma_i^{y0}$ , respectively. The current yield stress is taken as

$$\sigma_i^y(\kappa_i) = \sigma_i^{y0} + H_i \kappa_i(\bar{\rho}_i). \quad (32)$$

The hardening variable  $\kappa_i$  can be related to the normalized dislocation density,

$$\bar{\rho}_i = \frac{\rho_i}{\rho_i^0}, \quad (33)$$

through

$$\kappa_i = \sqrt{\bar{\rho}_i} - 1, \quad (34)$$

where  $\rho_i$  and  $\rho_i^0$  denotes the current and the initial dislocation density in grain  $i$ , respectively. Following Hallberg et al. [28] the evolution of the dislocation density is given by a classical Kocks-Mecking law of the form

$$\dot{\bar{\rho}}_i = (d_{1,i} \sqrt{\bar{\rho}_i} - d_{2,i} \bar{\rho}_i) \dot{\lambda}_i. \quad (35)$$

The model parameters  $d_{1,i}$  and  $d_{2,i}$  control the creation and annihilation of dislocations, respectively.

Combining Equations (24), (27) and (30), the dissipation potential becomes

$$\Omega(\pi^{dis}, \phi, c, \nabla \mu, \sigma, \mathbf{K}) = \frac{1}{2} L(\phi) \sum_i \left( \pi_i + \frac{\partial f}{\partial \phi_i} \right)^2 + \frac{1}{2} M(\phi) (\nabla \mu)^2 + \sum_i h_i(\phi) \Omega_{u,i}(c, \sigma_i, K_i). \quad (36)$$

### 2.4. Governing equations

Using the free energy (14), the state laws (7) become

$$\xi_i = \alpha \nabla \phi_i, \quad \mu = \tilde{\mu}, \quad \sigma = \sum_i h_i \mathbf{D}_i : (\epsilon - \epsilon_i^* - \epsilon_i^p). \quad (37)$$

To determine the chemical potential, it is enforced that all coexisting phases are in equilibrium under diffusive constraints, i.e.,

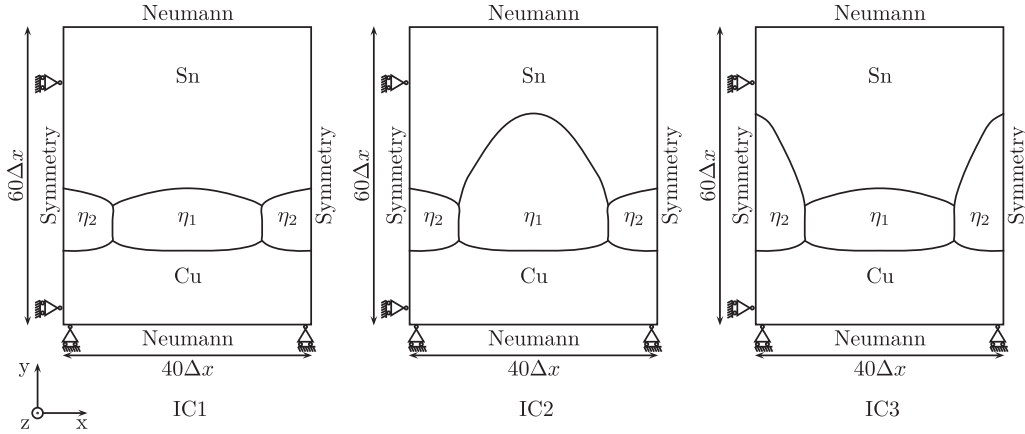


**Fig. 1.** Schematic representation of the initial microstructure and boundary conditions for the three model cases, IC1, IC2, and IC3. The computational domain is discretized using  $40 \times 60$  finite elements of size  $\Delta x = 50$  nm. IC1 corresponds to a microstructure obtained with a high cooling rate during reflow, which gives small scallop-shaped grain of IMC. IC2 and IC3 represent microstructures obtained with a low cooling rate, resulting in large IMC scallops.

$$\mu_i = \frac{\partial G_i}{\partial x_i} = \frac{\partial G_j}{\partial x_j} = \mu_j = \bar{\mu}. \quad (38)$$

The molar fraction of each phase must therefore be determined so that both mass balance (2) and equilibrium according to Equation (38) are fulfilled. Using the state laws and the dissipation potential (36), the diffusion flux (10) becomes

$$\mathbf{J} = -M(\phi) \nabla \bar{\mu}. \quad (39)$$

The evolution of the global molar concentration field follows the diffusion equation

$$\dot{c} = -\nabla \cdot \mathbf{J} = \nabla \cdot (M(\phi) \nabla \bar{\mu}). \quad (40)$$

From (9), the time derivative of phase field  $i$  is obtained as

$$\dot{\phi}_i = -L(\phi) \left( \pi_i + \frac{\partial f}{\partial \phi_i} \right). \quad (41)$$

In this equation the microforce  $\pi_i$  as well as  $\dot{\phi}_i$  are unknowns. Using the balance law for the microforces (3) and calculating the derivative  $\partial f / \partial \phi_i$ , the evolution equation for phase field  $i$  becomes

$$\begin{aligned} \dot{\phi}_i = L(\phi) & \left[ \nabla \cdot \alpha \nabla \phi_i - m \left( \phi_i^3 - \phi_i + 2\phi_i \sum_{j \neq i} \beta \phi_j^2 \right) \right. \\ & - \frac{2\phi_i}{\sum_k \phi_k^2} \left( (1 - h_i) (f_i^e + f_i^p) - \sum_{j \neq i} h_j (f_j^e + f_j^p) \right) \\ & \left. - \frac{2\phi_i}{\sum_k \phi_k^2} \left( (1 - h_i) \left( \frac{G_i}{V_m} - \frac{x_i}{V_m} \mu_i \right) - \sum_{j \neq i} h_j \left( \frac{G_j}{V_m} - \frac{x_j}{V_m} \mu_j \right) \right) \right], \end{aligned} \quad (42)$$

and analogously for the other phase fields.

### 3. Numerical implementation

The computational domain is represented by a regular grid of 41 by 61 nodal points and the weak form of (40) and (42) are

discretized in space using two-dimensional four-node finite elements of size  $\Delta x = \Delta y = 50$  nm and with bi-linear interpolation. Introducing the finite element approximations  $\phi_i = \mathbf{N} \bar{\phi}_i$  and  $\dot{c} = \mathbf{N} \dot{\bar{c}}$ , where  $\mathbf{N}$  contains the element shape functions, and choosing the weight function according to the Galerkin method yields the following FE-formulation of the evolution of the phase fields,

$$\begin{aligned} \int_V \mathbf{N}^T \mathbf{N} dV \dot{\bar{\phi}}_i = \int_S \mathbf{N}^T L(\phi) \alpha (\nabla \phi_i)^T \mathbf{n} dS - \int_V \mathbf{B}^T L(\phi) \alpha \nabla \phi_i dV \\ - \int_V \mathbf{N}^T L(\phi) \frac{\partial f}{\partial \phi_i} dV, \end{aligned} \quad (43)$$

and of the diffusion equation,

$$\int_V \mathbf{N}^T \mathbf{N} dV \dot{\bar{c}} = \int_S \mathbf{N}^T M(\phi) (\nabla \bar{\mu})^T \mathbf{n} dS - \int_V \mathbf{B}^T M(\phi) \nabla \bar{\mu} dV, \quad (44)$$

where  $\mathbf{B} = \nabla \mathbf{N}$  is the gradient of the shape functions. The time integration of Equations (43) and (44) can be performed efficiently using the Runge-Kutta-Chebyshev solver, RKC [29]. The RKC solver is intended for problems of the form  $\dot{y} = f(y, t)$ , however, (43) and (44) are of the form  $M \dot{y} = f(t, y)$ . To overcome this, the mass matrix  $M = \int_V \mathbf{N}^T \mathbf{N} dV$  is lumped into a vector by taking the sum over each row. The RKC solver is then used to integrate the problem  $\dot{y} = f(t, y)/M$ .

After each time step the non-linear mechanical equilibrium equation,

$$\int_V \tilde{\mathbf{B}}^T \boldsymbol{\sigma} dV = \mathbf{f}_{ext}, \quad (45)$$

where  $\tilde{\mathbf{B}}$  denotes the strain-displacement matrix, is solved using the Newton–Raphson scheme. In each iteration the plastic strains in all grains are updated using a radial return algorithm. In this work, the external force vector  $\mathbf{f}_{ext} = \mathbf{0}$  and the only loading included in the model comes from the applied transformation strain,  $\boldsymbol{\epsilon}^*$ .

To ensure that all coexisting phases are in thermodynamic equilibrium, the molar fraction field of each phase is updated so that Equations (2) and (38) are fulfilled. Using the parabolic approximations of the Gibbs free energy in (22) greatly simplifies this



**Table 1**

Material parameters used in the simulations. The mechanical parameters  $E$ ,  $\sigma^{y0}$ ,  $H$ ,  $d_1$ ,  $d_2$ , and  $\rho^0$  for Cu and Sn are calibrated from Refs. [33] and [34], respectively. The diffusion coefficients,  $D$ , are representative for the material behavior at 25° C.

		Cu	Cu <sub>6</sub> Sn <sub>5</sub>	Sn	Ref.
$E$ (GPa)	Young's modulus	150	112.3	19	[32]
$\nu$	Poisson's ratio	0.35	0.31	0.36	[18,35]
$\sigma^{y0}$ (MPa)	Initial yield stress	170		12	
$H$ (MPa)	Hardening modulus	0.69		0.75	
$d_1$	Creation of dislocations	1700		1400	
$d_2$	Annihilation of dislocations	12		80	
$\rho^0$ (m <sup>-2</sup> )	Initial dislocation density	$1.8 \times 10^{10}$		$48 \times 10^{10}$	
$\sigma_{int}$ (J m <sup>-2</sup> )	Surface energy	0.5	0.5	0.5	[15]
$D$ (m <sup>2</sup> s <sup>-1</sup> )	Bulk diffusion coefficient	$2.877 \times 10^{-36}$	$6.575 \times 10^{-19}$	$2.452 \times 10^{-17}$	[36]

task. For an interface where three phases coexist, the update of the molar fraction fields simply means that the system of equations,

$$\begin{bmatrix} \frac{h_i}{V_m} & \frac{h_j}{V_m} & \frac{h_k}{V_m} \\ A_i & -A_j & 0 \\ 0 & A_j & -A_k \end{bmatrix} \begin{bmatrix} x_i \\ x_j \\ x_k \end{bmatrix} = \begin{bmatrix} c \\ A_i \hat{x}_i - A_j \hat{x}_j + B_j - B_i \\ A_j \hat{x}_j - A_k \hat{x}_k + B_k - B_j \end{bmatrix}, \quad (46)$$

needs to be solved. For interfaces where more or fewer phases coexist, a similar system of equations can be constructed.

#### 4. Numerical example

The model described above is used to study the growth of the intermetallic compound Cu<sub>6</sub>Sn<sub>5</sub> during isothermal aging at room temperature (25° C). When a Cu substrate is in contact with liquid tin, for example during reflow soldering, scallop-shaped grains of Cu<sub>6</sub>Sn<sub>5</sub> will form at the interface [6]. The height and curvature of the scallops are affected by the solidification of the tin layer. Low cooling rates will lead to large scallops with greater curvature while faster cooling rates will give smaller scallops with less curvature [30]. To investigate the influence of the initial morphology of the Cu<sub>6</sub>Sn<sub>5</sub> layer on the growth behavior during aging, three cases have been studied. The model cases are illustrated in Fig. 1, where case 1 (IC1) represents a microstructure with small scallops, i.e. a high cooling rate, case 2 (IC2) and case 3 (IC3) represents microstructures with large scallops, i.e. a low cooling rate. In all cases, two grains of Cu<sub>6</sub>Sn<sub>5</sub> ( $\eta_1$  and  $\eta_2$ ) grow between one grain of Cu and one grain of Sn. In the Cu and Sn layers, the vertical boundaries of the computational domain can be seen as immobile grain boundaries. The difference between IC2 and IC3 is that the largest IMC scallop is growing in the bulk of the Sn grain for IC2 and in the grain boundary for IC3.

Symmetry boundary conditions for the phase fields and for the

concentration field are applied on the left and right boundaries of the domain. Homogeneous Neumann conditions are used at the top and bottom. The left side of the computational domain is held fixed in the horizontal direction and the bottom side is fixed in the vertical direction. The right boundary is free to move both horizontally and vertically, but with the horizontal displacements constrained so that the boundary remains straight. For simplicity it is assumed that the system is stress free at the start of the simulation.

#### 4.1. Choice of parameters

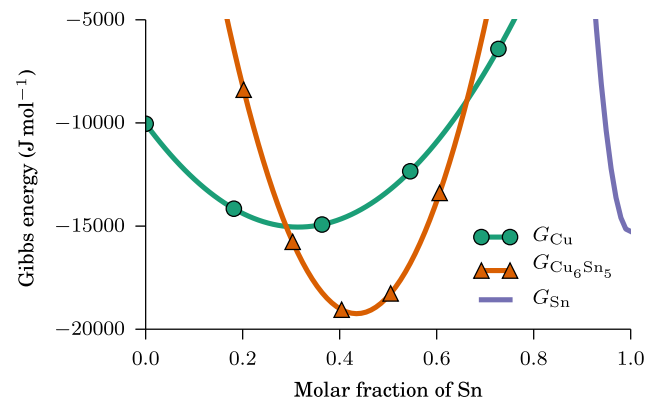
The model parameters  $m$ ,  $\alpha$  and  $\beta$  in the interface free energy (15) are functions of the surface energy  $\sigma_{int}$  and the width of the diffuse interface  $\delta$ . To properly resolve the interfaces, the diffuse interface region must include at least a few nodal points. In this work, the interface width is taken as  $\delta = 6\Delta x$  where  $\Delta x$  is the size of a finite element. We will also assume that all interfaces have the same surface energy, i.e., the model parameters  $m$ ,  $\alpha$  and  $\beta$  are taken as constant parameters.

The volume change associated with the growth of the IMC is simulated by applying a transformation strain to the newly formed intermetallic compound. Boettinger et al. [31] reports a lower bound of the transformation strain at  $\epsilon_{\eta}^* = -0.02$ , which would lead to tensile stresses in the IMC layer of about 4.8 GPa. Due to the brittle nature of intermetallic compounds, they are not expected to deform plastically. Since the yield stress of the Cu<sub>6</sub>Sn<sub>5</sub> phase is 2009 MPa [32], stresses of 4.8 GPa in the IMC layer are unphysical. In Ref. [31] it is therefore argued that reasonable values for the transformation strain are in the interval  $[0, -0.003]$ . A transformation strain of  $\epsilon_{\eta} = -0.003$  would give a decrease in volume of around 1% due to the formation of IMC. In reality this volume change is split into a volume expansion on the Sn side and a volume contraction on the Cu

**Table 2**

Thermodynamic data for Cu and Sn at 25° C, provided in Ref. [37] and coefficients obtained by fitting of parabolic functions. The two values for  $\hat{x}^{eq}$  for Cu<sub>6</sub>Sn<sub>5</sub> represents the equilibrium molar fraction of Cu<sub>6</sub>Sn<sub>5</sub> in contact with Cu and Sn, respectively.

	Cu	Cu <sub>6</sub> Sn <sub>5</sub>	Sn
$G^{\alpha}$ (J mol <sup>-1</sup> )	$-9.8837 \times 10^3$		$-1.2272 \times 10^4$
$G^{bct}$ (J mol <sup>-1</sup> )	$-3.9957 \times 10^3$		$-1.5259 \times 10^4$
$L_0^{\alpha}$ (J mol <sup>-1</sup> )	$-1.0888 \times 10^4$		
$L_1^{\alpha}$ (J mol <sup>-1</sup> )	$-1.1270 \times 10^4$		
$A$ (J mol <sup>-1</sup> )	$1.0133 \times 10^5$	$4.0 \times 10^5$	$4.2059 \times 10^6$
$B$ (J mol <sup>-1</sup> )	$-2.1146 \times 10^4$	$-6.9892 \times 10^3$	$7.1680 \times 10^3$
$C$ (J mol <sup>-1</sup> )	$-1.2842 \times 10^4$	$-1.9185 \times 10^4$	$-1.5265 \times 10^4$
$\hat{x}$	0.105 69	0.41753	0.99941
$\hat{x}^{eq}$	0.105 69	0.38210/0.452 90	0.99941

**Fig. 2.** Gibbs energy curves for all phases at 25° C.

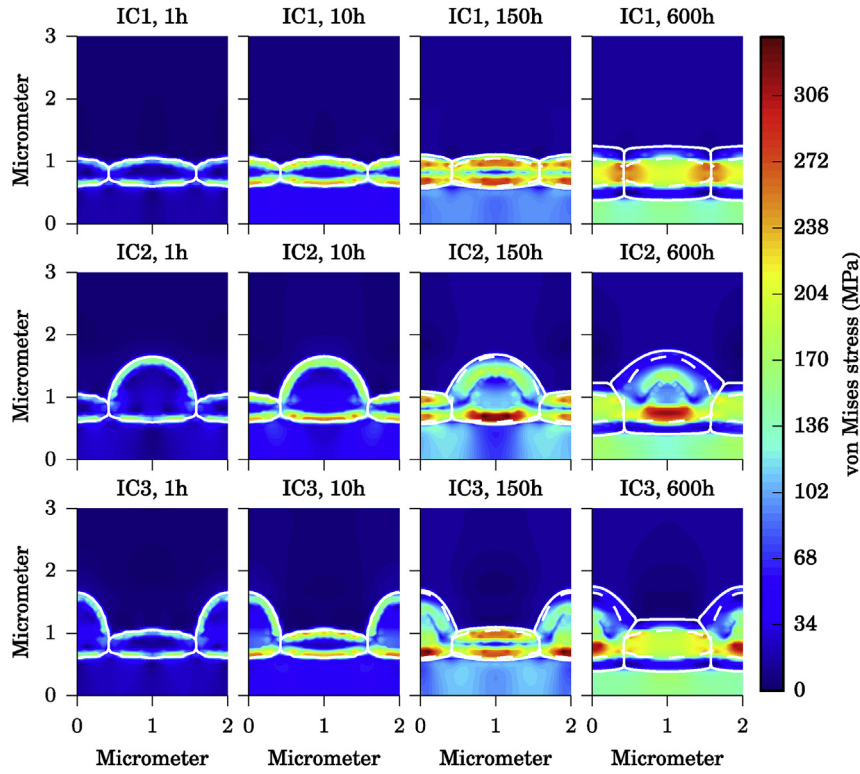


**Fig. 3.** Evolution of the microstructure and the von Mises stress for the three different initial condition and using  $D_{gb} = 1000D_\eta$ . The dashed and solid contours corresponds to the initial and the current position of grain boundaries, respectively. Top row: Initial condition 1, IC1. Middle row: Initial condition 2, IC2. Bottom row: Initial condition 3, IC3.

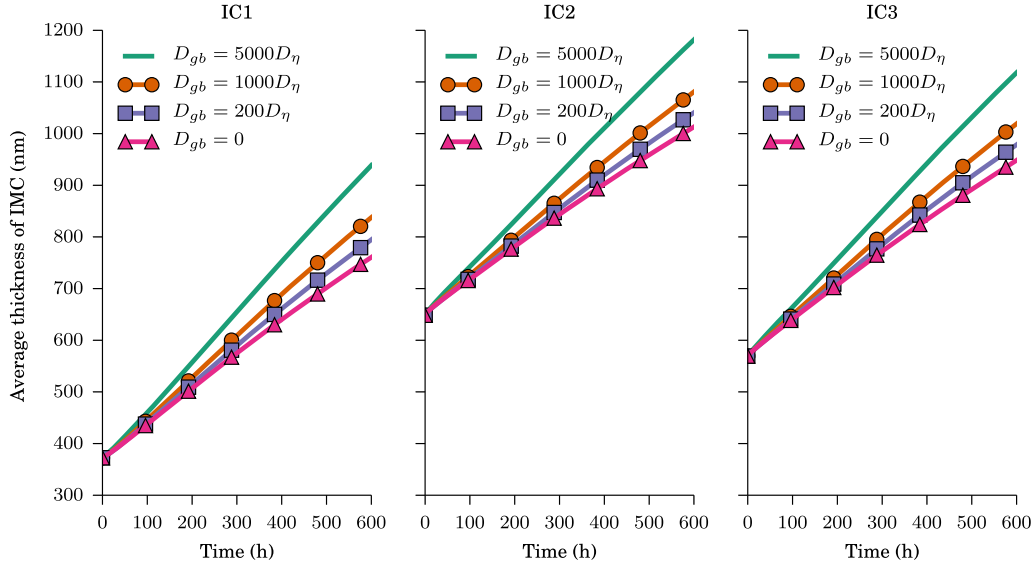


**Fig. 4.** Average thickness of the IMC layer as a function of time for simulations with different values of  $D_{gb}$ . Left: initial condition 1, IC1. Center: Initial condition 2, IC2. Right: Initial condition 3, IC3.

**Table 3**

Growth rates of the  $\text{Cu}_6\text{Sn}_5$  obtained from simulations with the three initial conditions IC1, IC2, and IC3 and using different values for the grain boundary diffusion coefficient  $D_{gb}$ .

	IC1 (nm h <sup>-1</sup> )	IC2 (nm h <sup>-1</sup> )	IC3 (nm h <sup>-1</sup> )
$D_{gb} = 0$	0.66	0.60	0.63
$D_{gb} = 200D_\eta$	0.72	0.65	0.68
$D_{gb} = 1000D_\eta$	0.79	0.72	0.75
$D_{gb} = 5000D_\eta$	0.96	0.89	0.92

side. For simplicity, we take the transformation strain as  $\epsilon_i^* = [\epsilon_{xx}^* \ \epsilon_{yy}^* \ \epsilon_{xy}^*]^T = -0.003[1 \ 1 \ 0]^T$  for the IMC grains and  $\epsilon_i^* = \mathbf{0}$  for the other grains.

The plasticity model described by Equations (31)–(35) have been calibrated to experiments by Champion et al. [33] for the Cu phase and by Amagai et al. [34] for the Sn phase, respectively. In addition, the parameters are calibrated so that the hardening behavior, (32), matches the behavior predicted by the Taylor equation,

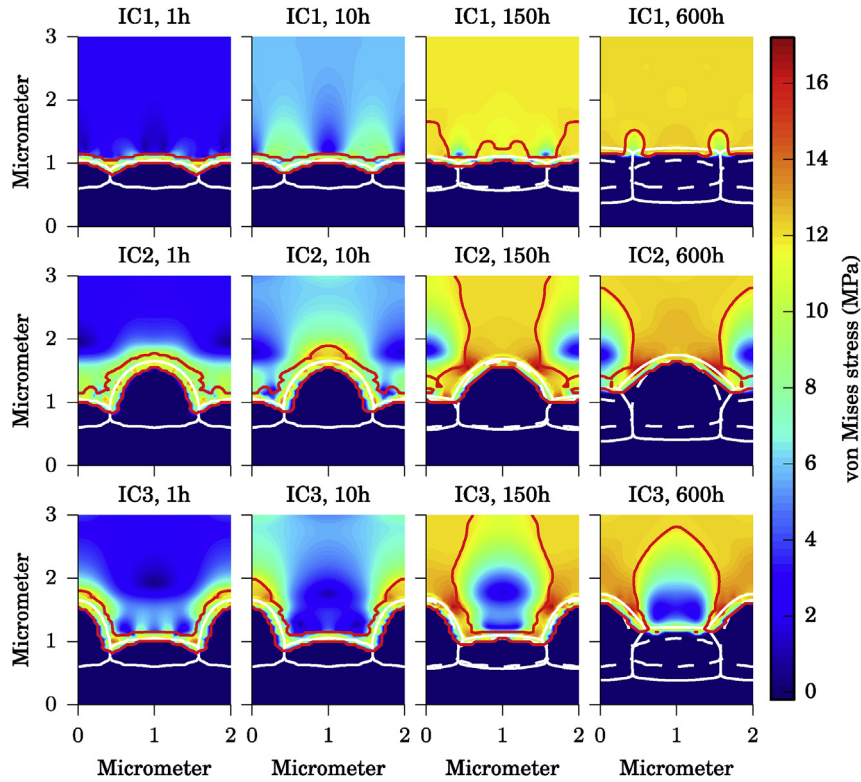


**Fig. 5.** Evolution of the von Mises stress in the Sn layer for the three different initial conditions and using  $D_{gb} = 1000D_\eta$ . The stress in the Cu and IMC layers has been removed for display purpose. The red contour indicates the region inside which the relative dislocation density is greater than 1, i.e., the zone where the dislocation density has evolved under plastic deformation. The dashed and solid white contours corresponds to the initial and the current position of grain boundaries, respectively. Top row: Initial condition 1, IC1. Middle row: Initial condition 2, IC2. Bottom row: Initial condition 3, IC3. (For interpretation of the references to color in this figure legend, the reader is referred to the web version of this article.)

$$\sigma_i^y = \sigma_i^{y0} + \alpha \mu b \sqrt{\rho_i \rho_i^0}, \quad (47)$$

where  $\alpha = 0.35$  is a parameter related to the strength of dislocation interactions,  $\mu$  is the shear modulus and  $b$  is the magnitude of the Burgers vector, taken as  $b = 0.256$  nm for Cu and  $b = 0.412$  nm for Sn. The resulting parameters are presented in Table 1.

The kinetic coefficient  $L_{ab}$ , as calculated using (29), only applies to interfaces between grains of different phases. For interfaces between grains of the same phase, the kinetic coefficient relates to the grain boundary mobility  $m_{ii}$  according to [15],

$$L_{ii} = \frac{m_{ii} \sigma_{ii}}{\alpha_{ii}}. \quad (48)$$

Due to a lack of experimental data on the grain boundary mobility of  $\text{Cu}_6\text{Sn}_5$  it is assumed that  $L_{\eta\eta} = L_{\eta\text{Cu}}$ .

The initial molar fractions and the molar volume are taken as  $x_{\text{Cu}} = 0.200\%$ ,  $x_\eta = 41.7\%$ ,  $x_{\text{Sn}} = 99.9\%$ , and  $V_m = 16.29 \text{ cm}^3 \text{ mol}^{-1}$ , respectively. Other parameters used in the simulations are given in Table 1.

#### 4.2. Approximation of Gibbs energy

The composition dependence of the Gibbs energy in the Cu and Sn phases can be described, using the substitutional model [37], by

$$\begin{aligned} \hat{G}_m^p(T, x) = & (1-x)G_{\text{Cu}}^p(T) + xG_{\text{Sn}}^p(T) + RT[(1-x)\ln(1-x) \\ & + x \ln x] + x(1-x) \sum_j L_j^p(T)(1-2x)^j, \end{aligned} \quad (49)$$

where  $x$  is the molar fraction of Sn,  $R$  is the gas constant,  $T$  is the temperature and  $G_{\text{Cu}}^p$ ,  $G_{\text{Sn}}^p$  and  $L_j^p$  are the Gibbs energy and the interaction parameters for the pure element of phase  $p$ , respectively. The Gibbs energy of  $\text{Cu}_6\text{Sn}_5$  is taken according to [16,38] as

$$\begin{aligned} \hat{G}_\eta(T, x) = & 2 \times 10^5 (x - \hat{x}_\eta)^2 + 0.545G_{\text{Cu}}^\alpha + 0.455G_{\text{Sn}}^{bct} - 6869.5 \\ & - 0.1589T. \end{aligned} \quad (50)$$

The first term in (50) is added to introduce a composition dependency to the otherwise constant Gibbs energy of the intermetallic phase. To obtain the Gibbs energy curves used in the phase field model, parabolas of the form (22) are fitted to (49) and (50). The thermodynamic parameters used and the coefficients of the fitted parabolas are presented in Table 2. The fitted curves are shown in Fig. 2.

## 5. Results and discussion

### 5.1. Evolution of the microstructure

In Fig. 3 the evolution of the microstructure is shown for simulations with IC1, IC2, and IC3. The solid white contour lines correspond to the position of the grain boundaries, represented by



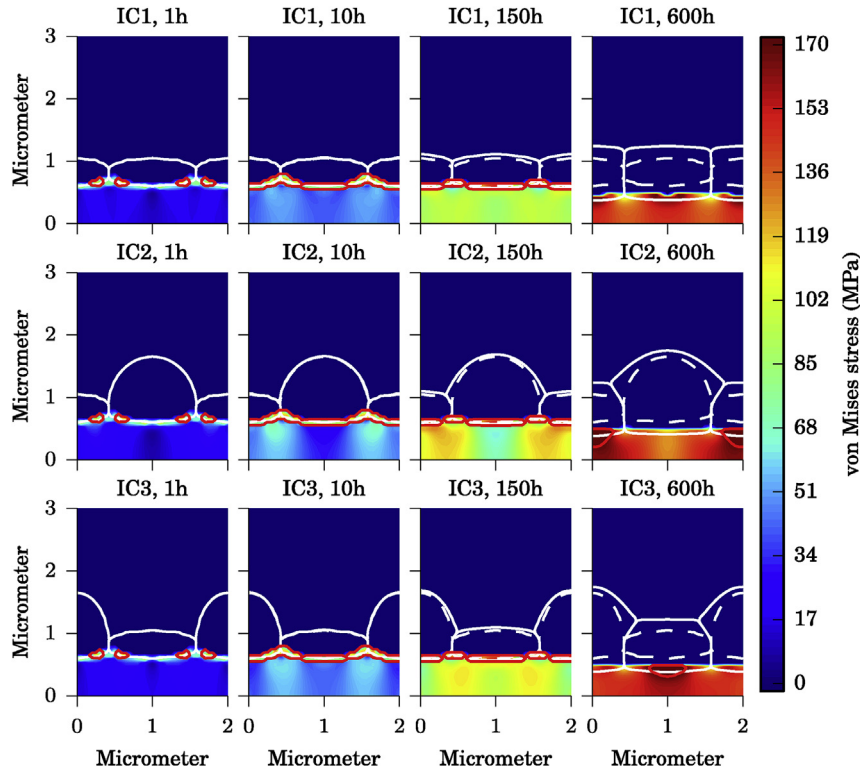


**Fig. 6.** Evolution of the von Mises stress in the Cu layer for the three different initial conditions and using  $D_{gb} = 1000D_\eta$ . The stress in the Sn and IMC layers has been removed for display purpose. The red contour indicates the region inside which the relative dislocation density is greater than 1, i.e., the zone where the dislocation density has evolved under plastic deformation. The dashed and solid white contours corresponds to the initial and the current position of grain boundaries, respectively. Top row: Initial condition 1, IC1. Middle row: Initial condition 2, IC2. Bottom row: Initial condition 3, IC3. (For interpretation of the references to color in this figure legend, the reader is referred to the web version of this article.)

the level set  $h_\eta = 0.5$ , at times 1 h, 10 h, 150 h, and 600 h. The dashed white contour lines represent the initial position of the grain boundaries. The colormap of Fig. 3 corresponds to the von Mises stress and will be discussed in the next section. In all simulations the grain boundary diffusion coefficient is taken as  $D_{gb} = 1000D_\eta$ . For all initial conditions it is seen that the IMC layer grows thicker with time. Initially, due to the faster diffusion in Sn, the IMC grows primarily into the Sn layer, at a later stage, growth takes place at the Cu side as well. In all simulations, the initially scallop-shaped interface between  $\text{Cu}_6\text{Sn}_5$  and Sn gradually transitions into a more planar morphology. This behavior has been observed experimentally during solid state aging of tin at different temperatures below the melting temperature [12,39,40]. During aging, the grain boundaries between the IMC grains remain vertical for IC1, whereas for IC2 and IC3, due to different IMC grain sizes, curved grain boundaries are obtained.

To study the effect of grain boundary diffusion on the growth of the IMC layer, simulations with different values of the grain boundary diffusion coefficient  $D_{gb}$  have been performed. In Fig. 4 the average thickness of the IMC layer is plotted as a function of time for simulations with  $D_{gb} = 0$ ,  $D_{gb} = 200D_\eta$ ,  $D_{gb} = 1000D_\eta$ , and  $D_{gb} = 5000D_\eta$  for all three initial conditions. The growth of the IMC layer is almost linear for all simulations, however, a slight decrease in growth rate with time is observed. In Table 3 the growth rates of the simulations are presented. It is seen that the highest growth rates are obtained for the simulation with  $D_{gb} = 5000D_\eta$ . In addition, for any given value of  $D_{gb}$ , the growth rate is lowest for IC2 and highest for IC1. This observation is explained by the IMC acting as a diffusion barrier between the Cu and the Sn layers, so a thicker IMC layer (i.e. IC2) will grow slower as the diffusion distance is larger. For the same reason the growth rate decreases towards the end of

the simulations. Whilst only a few experimental studies have been performed on the room-temperature growth of  $\text{Cu}_6\text{Sn}_5$ , Tu and Thompson report growth rates of  $0.15 \text{ nm h}^{-1}$  and  $0.25 \text{ nm h}^{-1}$  for two different samples [41]. However, a growth rate of around  $2.3 \text{ nm h}^{-1}$  is obtained from the data in Ref. [8]. The large discrepancy in the growth rates reported in literature makes it hard to quantitatively verify the results from simulations. Nonetheless, by comparing the experimental results with the values in Table 3, we can conclude that the growth rate from the simulations are in the correct range. We also conclude that the simulations show the same tendencies as the experiments, both regarding the linear growth and the transition from scallop-shaped to plane interface morphology.

## 5.2. Mechanical behavior

From Fig. 3 we can see that the growth of the IMC generates stress in the IMC layer. Initially, the highest stress is found in the interface regions where a volume change occurs due to the transformation strain. With time, the stress in the center of the IMC layer becomes dominant and the stress in the interface regions decrease. The highest stress in the IMC layer is found below the large scallop in IC2 and IC3. The stress level is around 300 MPa which is well below the yield stress reported in Ref. [32], thus validating the assumption of only elastic deformation in the IMC.

Due to the negative volume change associated with the formation of IMC, a compaction of the surrounding microstructure takes place and we expect compressive stress to develop in the Cu and the Sn layers. In Figs. 5 and 6 the evolution of the von Mises stress in the Cu and Sn layers are plotted for the three initial conditions. Note that in Figs. 5 and 6 the stress in the Cu/Sn and IMC layers has been

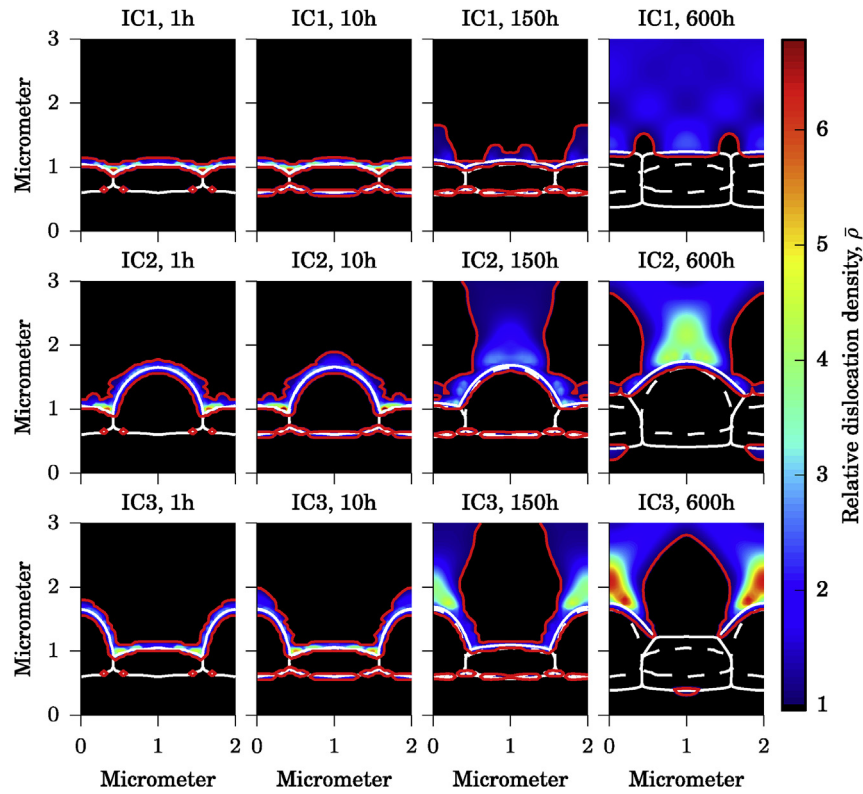


**Fig. 7.** Evolution of the dislocation density in the Sn and Cu layers for the three different initial conditions and using  $D_{gb} = 1000D_{\eta}$ . The red contour indicates the region inside which the relative dislocation density is greater than 1, i.e., the zone where the dislocation density has evolved under plastic deformation. The dashed and solid white contours corresponds to the initial and the current position of grain boundaries, respectively. Top row: Initial condition 1, IC1. Middle row: Initial condition 2, IC2. Bottom row: Initial condition 3, IC3. (For interpretation of the references to color in this figure legend, the reader is referred to the web version of this article.)

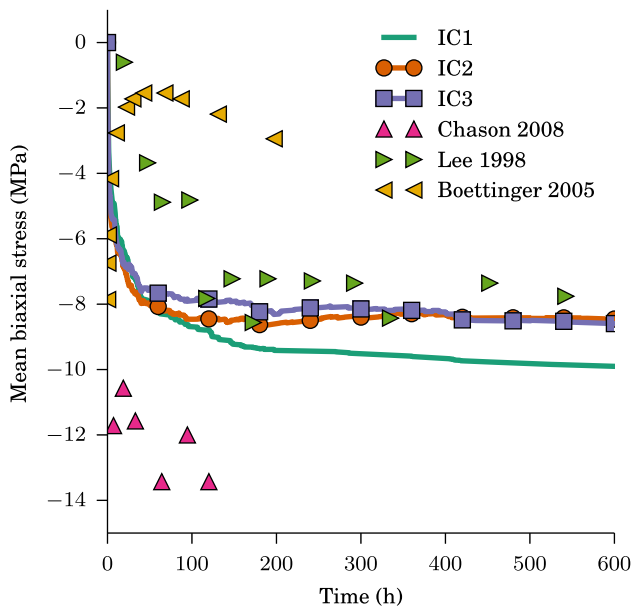


**Fig. 8.** Mean biaxial stress as a function of time for the three initial conditions using  $D_{gb} = 1000D_{\eta}$ . The experimental data is taken from Refs. [8,31,42].

removed for display purposes. In the figures the red contour indicates the region where the normalized dislocation density,  $\bar{\rho}$ , is greater than 1, i.e. the zone where plastic deformation takes place by evolution of the dislocation density. For IC1, cf. Fig. 5, the stress in the Sn layer is initially concentrated in the region close to the

interface. With time, the stress spreads throughout the Sn layer and the stress field becomes almost homogenous. We also see that a plastic zone forms near the interface between IMC and Sn and grows larger with time. At the end of the simulation, for IC1, the whole Sn layer, except a small region above the grain boundaries between the IMC grains, is plastically deformed. At the start of the simulation, for IC2 and IC3, the elevated stress spreads further into the Sn layer than for IC1 and the initial plastic zone is larger. The growth of the plastic zone takes place mainly above the large IMC scallop, i.e., in the center for IC2 and along the boundaries for IC3. Outside the plastic zone a nearly stress free region is found in both IC2 and IC3.

The von Mises stress in the Cu layer for the three initial cases is shown in Fig. 6. Since the interface between Cu and IMC are identical for all three initial cases the stress fields are very similar. It is seen that the stress is slightly higher in the regions below the grain boundaries.

In Fig. 7 the evolution of the dislocation density in the Cu and the Sn layer is shown. On the Cu side, plasticity is initiated in several regions along the interface for all initial conditions. These regions merge at a later stage and the plastic zone expands to cover the whole interface. The plastic zone gets consumed by the growing IMC layer during further aging and only a small plastic zone is found in the Cu layer at the end of the simulation. In the Sn layer we see that most dislocations are created around the grain boundary regions and around the large IMC scallop. It is also seen that the dislocation density is lower in IC1 than it is in IC2 and IC3. This indicates that the curvature of the IMC layer plays a role in the evolution of the dislocation density. Furthermore, the dislocation density is highest in IC3, which indicates that dislocations are more easily generated when IMC scallops grow in the grain boundaries

between Sn grains (in the simulations these are represented by the lateral boundaries of the computational domain). We also see that the level of the dislocation density is much higher in the Sn layer than in the Cu layer.

In Fig. 8 the mean biaxial stress in the Sn layer is plotted as a function of time for the three initial conditions in addition to experimental data from Refs. [8,31,42]. The mean biaxial stress, in Fig. 8, is calculated as

$$\bar{\sigma}_{biax} = \frac{1}{2}(\bar{\sigma}_{xx} + \bar{\sigma}_{zz}), \quad (51)$$

where  $\bar{\sigma}_{xx}$  and  $\bar{\sigma}_{zz}$  are the volume averaged stresses in the x- and z-direction, respectively. From Fig. 8 it is seen that, for all initial conditions, the mean biaxial stress becomes increasingly compressive with time until it reaches a minimum value of  $-8$  MPa to  $-10$  MPa after approximately 150 h of aging. During further aging the biaxial stress remains almost constant, which indicates that the growth of the IMC grains is accommodated by plastic deformation of the Sn layer. The curves for IC2 and IC3 are very similar, this is expected as the only difference between the two cases is the location of the large scallop. For IC1, the magnitude of the biaxial stress is slightly higher than for the other cases. The predicted stresses are in very good agreement with the experimental data presented in Ref. [42], but slightly smaller in magnitude than the data in Ref. [8] and slightly larger in magnitude than the data in Ref. [31]. It should be noted that the experiments of [31,42] and [8] were performed on Sn layers of different thicknesses and the stress is expected to be higher in magnitude for thinner Sn layers.

## 6. Conclusions

A multiphase field model taking into account fast diffusion in grain boundaries as well as elastoplastic material behavior has been developed. The governing equations of the model have been derived in a thermodynamically consistent way in a multiphase setting. The model approach allows different constitutive laws to be associated with different phase fields, thus extending the applicability of the model. In the present work, the model has been used to study the growth of the intermetallic compound  $\text{Cu}_6\text{Sn}_5$  during room-temperature aging for three different initial microstructures. An isotropic von Mises plasticity model with hardening based on the dislocation density has been used for the Cu and Sn phases, while the IMC was assumed to behave elastically. It was found that the model qualitatively captures the transition from a scallop-like to a layered IMC morphology [12,39,40] and the linear growth dependence on time [8,41], as seen in experiments. We have also shown that the growth rate of the IMC depends on the grain boundary diffusion coefficient, a higher value will increase the grain boundary mobility and give a higher growth rate. Furthermore, the model predicted that the volume change associated with the growing  $\text{Cu}_6\text{Sn}_5$  layer gives rise to stress in the IMC as well as in the Cu and the Sn layers. It was also found that the Cu and Sn layers both deformed plastically. For all initial microstructures, a large part of the Sn layer deformed plastically and most dislocations were created around the larger IMC scallops. The plastic zone in the Cu layer was found to be smaller and more concentrated to the interface region for all initial conditions. The evolution of the mean biaxial stress predicted by the model is in good agreement with experimental data and indicates that the growth of the IMC layer is accommodated by plastic deformation of the Sn layer.

## Acknowledgments

The authors gratefully acknowledge the funding provided by the Swedish Research Council (Vetenskapsrådet, VR) under grant 2011-5512. H. Hallberg also gratefully acknowledges funding from the same organization under grant 2012-4231.

## References

- [1] N. Moelans, B. Blanpain, P. Wollants, An introduction to phase-field modeling of microstructure evolution, *Calphad* 32 (2) (2008) 268–294, <http://dx.doi.org/10.1016/j.calphad.2007.11.003>.
- [2] W. Boettinger, J. Warren, C. Beckermann, A. Karma, Phase-field simulation of solidification, *Annu. Rev. Mater. Res.* 32 (1) (2002) 163–194, <http://dx.doi.org/10.1146/annurev.matsci.32.101901.155803>.
- [3] A. Karma, W.-J. Rappel, Quantitative phase-field modeling of dendritic growth in two and three dimensions, *Phys. Rev. E* 57 (4) (1998) 4323, <http://dx.doi.org/10.1103/PhysRevE.57.4323>.
- [4] T. Takaki, Y. Hisakuni, T. Hirouchi, A. Yamanaka, Y. Tomita, Multi-phase-field simulations for dynamic recrystallization, *Comput. Mater. Sci.* 45 (4) (2009) 881–888, <http://dx.doi.org/10.1016/j.commatsci.2008.12.009>.
- [5] A. Artemev, Y. Jin, A. Khachaturyan, Three-dimensional phase field model of proper martensitic transformation, *Acta Mater.* 49 (7) (2001) 1165–1177, [http://dx.doi.org/10.1016/S1359-6454\(01\)00021-0](http://dx.doi.org/10.1016/S1359-6454(01)00021-0).
- [6] M. Yang, M. Li, C. Wang, Interfacial reactions of eutectic  $\text{Sn3.5Ag}$  and pure tin solders with Cu substrates during liquid-state soldering, *Intermetallics* 25 (0) (2012) 86–94, <http://dx.doi.org/10.1016/j.intermet.2012.02.023>.
- [7] A. He, D. Ivey, Microstructural study of Sn films electrodeposited on Cu substrates: Sn whiskers and  $\text{Cu}_6\text{Sn}_5$  precipitates, *J. Mater. Sci.* 50 (7) (2015) 2944–2959, <http://dx.doi.org/10.1007/s10853-015-8859-6>.
- [8] E. Chason, N. Jadhav, W. Chan, L. Reinbold, K. Kumar, Whisker formation in Sn and Pb–Sn coatings: role of intermetallic growth, stress evolution, and plastic deformation processes, *Appl. Phys. Lett.* 92 (17) (2008) 171901, <http://dx.doi.org/10.1063/1.2912528>.
- [9] J. Gong, C. Liu, P.P. Conway, V.V. Silberschmidt, Evolution of CuSn intermetallics between molten SnAgCu solder and Cu substrate, *Acta Mater.* 56 (16) (2008) 4291–4297, <http://dx.doi.org/10.1016/j.actamat.2008.04.063>.
- [10] C.-P. Lin, C.-M. Chen, Y.-W. Yen, Enhanced growth of the  $\text{Cu}_6\text{Sn}_5$  phase in the Sn/Ag/Cu and Sn/Cu multilayers subjected to applied strain, *J. Alloys Compd.* 591 (2014) 297–303, <http://dx.doi.org/10.1016/j.jallcom.2013.12.204>.
- [11] S. Choi, T. Bieler, J. Lucas, K. Subramanian, Characterization of the growth of intermetallic interfacial layers of Sn–Ag and Sn–Pb eutectic solders and their composite solders on Cu substrate during isothermal long-term aging, *J. Electron. Mater.* 28 (11) (1999) 1209–1215, <http://dx.doi.org/10.1007/s11664-999-0159-y>.
- [12] M. Yang, H. Chen, X. Ma, M. Li, Y. Cao, J. Kim, Solid-state interfacial reaction of eutectic  $\text{Sn3.5Ag}$  and pure tin solders with polycrystalline Cu substrate, *J. Mater. Sci.* 49 (10) (2014) 3652–3664, <http://dx.doi.org/10.1007/s10853-014-8069-7>.
- [13] H. Kim, K. Tu, Kinetic analysis of the soldering reaction between eutectic SnPb alloy and Cu accompanied by ripening, *Phys. Rev. B* 53 (23) (1996) 16027, <http://dx.doi.org/10.1103/PhysRevB.53.16027>.
- [14] J. Huh, K. Hong, Y. Kim, K. Kim, Phase field simulations of intermetallic compound growth during soldering reactions, *J. Electron. Mater.* 33 (10) (2004) 1161–1170, <http://dx.doi.org/10.1007/s11664-004-0118-6>.
- [15] N. Moelans, A quantitative and thermodynamically consistent phase-field interpolation function for multi-phase systems, *Acta Mater.* 59 (3) (2011) 1077–1086, <http://dx.doi.org/10.1016/j.actamat.2010.10.038>.
- [16] M. Park, R. Arróyave, Early stages of intermetallic compound formation and growth during lead-free soldering, *Acta Mater.* 58 (14) (2010) 4900–4910, <http://dx.doi.org/10.1016/j.actamat.2010.05.028>.
- [17] A. Umantsev, Modeling of intermediate phase growth, *J. Appl. Phys.* 101 (2) (2007) 024910, <http://dx.doi.org/10.1063/1.2424530>.
- [18] E. Buchovecky, N. Jadhav, A.F. Bower, E. Chason, Finite element modeling of stress evolution in Sn films due to growth of the  $\text{Cu}_6\text{Sn}_5$  intermetallic compound, *J. Electron. Mater.* 38 (12) (2009) 2676–2684, <http://dx.doi.org/10.1007/s11664-009-0911-3>.
- [19] P.G. Harris, K.S. Chaggar, The role of intermetallic compounds in lead-free soldering, *Solder. Surf. Mt. Technol.* 10 (3) (1998) 38–52, <http://dx.doi.org/10.1108/09540919810237110>.
- [20] G.T. Galyon, Annotated tin whisker bibliography and anthology, *IEEE Trans. Electron. Packag. Manuf.* 28 (1) (2005) 94–122, <http://dx.doi.org/10.1109/TEPM.2005.847440>.
- [21] E. Fried, M.E. Gurtin, Dynamic solid–solid transitions with phase characterized by an order parameter, *Phys. D. Nonlinear Phenom.* 72 (4) (1994) 287–308, [http://dx.doi.org/10.1016/0167-2789\(94\)90234-8](http://dx.doi.org/10.1016/0167-2789(94)90234-8).
- [22] M.E. Gurtin, Generalized Ginzburg–Landau and Cahn–Hilliard equations based on a microforce balance, *Phys. D. Nonlinear Phenom.* 92 (3) (1996) 178–192, [http://dx.doi.org/10.1016/0167-2789\(95\)00173-5](http://dx.doi.org/10.1016/0167-2789(95)00173-5).
- [23] K. Ammar, B. Appolaire, G. Caillaud, S. Forest, Combining phase field approach and homogenization methods for modelling phase transformation in elastoplastic media, *Eur. J. Comput. Mech. Rev. Eur. de Méc. Numér.* 18

- (5–6) (2009) 485–523, <http://dx.doi.org/10.3166/EJCM.18.485-523>.
- [24] R. Hill, Elastic properties of reinforced solids: some theoretical principles, *J. Mech. Phys. Solids* 11 (5) (1963) 357–372, [http://dx.doi.org/10.1016/0022-5096\(63\)90036-X](http://dx.doi.org/10.1016/0022-5096(63)90036-X).
- [25] A. Khachaturyan, *Theory of Structural Phase Transformations in Solids*, vol. 17, John Wiley, New York, NY, 1983.
- [26] K. Ammar, B. Appolaire, S. Forest, M. Cottura, Y. Le Bouar, A. Finel, Modelling inheritance of plastic deformation during migration of phase boundaries using a phase field method, *Meccanica* 49 (11) (2014) 2699–2717, <http://dx.doi.org/10.1007/s11012-014-0011-1>.
- [27] Y. Guan, N. Moelans, Influence of the solubility range of intermetallic compounds on their growth behavior in hetero-junctions, *J. Alloys Compd.* 635 (2015) 289–299, <http://dx.doi.org/10.1016/j.jallcom.2015.02.028>.
- [28] H. Hallberg, M. Wallin, M. Ristinmaa, Modeling of continuous dynamic recrystallization in commercial-purity aluminum, *Mater. Sci. Eng. A* 527 (4) (2010) 1126–1134, <http://dx.doi.org/10.1016/j.msea.2009.09.043>.
- [29] B. Sommeijer, L. Shampine, J. Verwer, RKC: an explicit solver for parabolic PDEs, *J. Comput. Appl. Math.* 88 (2) (1998) 315–326, [http://dx.doi.org/10.1016/S0377-0427\(97\)00219-7](http://dx.doi.org/10.1016/S0377-0427(97)00219-7).
- [30] X. Deng, G. Piotrowski, J. Williams, N. Chawla, Influence of initial morphology and thickness of  $\text{Cu}_6\text{Sn}_5$  and  $\text{Cu}_3\text{Sn}$  intermetallics on growth and evolution during thermal aging of Sn–Ag solder/Cu joints, *J. Electron. Mater.* 32 (12) (2003) 1403–1413, <http://dx.doi.org/10.1007/s11664-003-0108-0>.
- [31] W. Boettinger, C. Johnson, L. Bendersky, K.-W. Moon, M. Williams, G. Stafford, Whisker and hillock formation on Sn, Sn–Cu and Sn–Pb electrodeposits, *Acta Mater.* 53 (19) (2005) 5033–5050, <http://dx.doi.org/10.1016/j.actamat.2005.07.016>.
- [32] X. Deng, N. Chawla, K. Chawla, M. Koopman, Deformation behavior of (Cu, Ag)–Sn intermetallics by nanoindentation, *Acta Mater.* 52 (14) (2004) 4291–4303, <http://dx.doi.org/10.1016/j.actamat.2004.05.046>.
- [33] Y. Champion, C. Langlois, S. Guérin-Mailly, P. Langlois, J.-L. Bonnentien, M.J. Hytch, Near-perfect elastoplasticity in pure nanocrystalline copper, *Science* 300 (5617) (2003) 310–311, <http://dx.doi.org/10.1126/science.1081042>.
- [34] M. Amagai, M. Watanabe, M. Omiya, K. Kishimoto, T. Shibuya, Mechanical characterization of Sn–Ag-based lead-free solders, *Microelectron. Reliab.* 42 (6) (2002) 951–966, [http://dx.doi.org/10.1016/S0026-2714\(02\)00017-3](http://dx.doi.org/10.1016/S0026-2714(02)00017-3).
- [35] H. Qin, X. Zhang, M. Zhou, X. Li, Y.-W. Mai, Geometry effect on mechanical performance and fracture behavior of micro-scale ball grid array structure Cu/Sn–3.0 Ag–0.5 Cu/Cu solder joints, *Microelectron. Reliab.* 55 (8) (2015) 1214–1225, <http://dx.doi.org/10.1016/j.microrel.2015.05.013>.
- [36] Z. Mei, A. Sunwoo, J. Morris, Analysis of low-temperature intermetallic growth in copper–tin diffusion couples, *Metall. Trans. A* 23 (3) (1992) 857–864, <http://dx.doi.org/10.1007/BF02675563>.
- [37] M. Li, Z. Du, C. Guo, C. Li, Thermodynamic optimization of the Cu–Sn and Cu–Nb–Sn systems, *J. Alloys Compd.* 477 (1) (2009) 104–117, <http://dx.doi.org/10.1016/j.jallcom.2008.09.141>.
- [38] J.-H. Shim, C.-S. Oh, B.-J. Lee, D. Lee, Thermodynamic assessment of the Cu–Sn system, *Z. für Met.* 87 (3) (1996) 205–212.
- [39] J. Shen, Z. Cao, D. Zhai, M. Zhao, P. He, Effect of isothermal aging and low density current on intermetallic compound growth rate in lead-free solder interface, *Microelectron. Reliab.* 54 (1) (2014) 252–258, <http://dx.doi.org/10.1016/j.microrel.2013.09.005>.
- [40] T. Lee, W. Choi, K. Tu, J. Jang, S. Kuo, J. Lin, D. Frear, K. Zeng, J. Kivilahti, Morphology, kinetics, and thermodynamics of solid-state aging of eutectic SnPb and Pb-free solders (Sn–3.5Ag, Sn–3.8Ag–0.7Cu and Sn–0.7Cu) on Cu, *J. Mater. Res.* 17 (02) (2002) 291–301, <http://dx.doi.org/10.1557/JMR.2002.0042>.
- [41] K. Tu, R. Thompson, Kinetics of interfacial reaction in bimetallic Cu–Sn thin films, *Acta Metall.* 30 (5) (1982) 947–952, [http://dx.doi.org/10.1016/0001-6160\(82\)90201-2](http://dx.doi.org/10.1016/0001-6160(82)90201-2).
- [42] B.-Z. Lee, D. Lee, Spontaneous growth mechanism of tin whiskers, *Acta Mater.* 46 (10) (1998) 3701–3714, [http://dx.doi.org/10.1016/S1359-6454\(98\)00045-7](http://dx.doi.org/10.1016/S1359-6454(98)00045-7).